AGU ADVANCING EARTH AND SPACE SCIENCE

Geophysical Research Letters®

RESEARCH LETTER
10.1029/2022GL099449

Key Points:

- Boundaries and their convection over Hetao Irrigation District prefer mid-level high-pressure-ridge or pre-trough synoptic patterns
- The favorable patterns have a warmer boundary layer with more frequent southerly flows, larger CAPE, and stronger moisture convergence
- Instability and moisture effectively distinguish convective from nonconvective boundary days but not boundary from nonboundary days

Supporting Information:

Supporting Information may be found in the online version of this article.

Correspondence to:

Z. Meng,
zymeng@pku.edu.cn

Citation:

Huang, Y., Meng, Z., & Zhang, M. (2022). Synoptic impacts on the occurrence of mesoscale boundaries and their associated convection over an area of sharp vegetation contrast. *Geophysical Research Letters*, *49*, e2022GL099449. https://doi.org/10.1029/2022GL099449

Received 10 MAY 2022
Accepted 5 AUG 2022

Synoptic Impacts on the Occurrence of Mesoscale Boundaries and Their Associated Convection Over an Area of Sharp Vegetation Contrast

Yipeng Huang[1], Zhiyong Meng[2], and Murong Zhang[3]

[1]Xiamen Key Laboratory of Straits Meteorology, Xiamen Meteorological Bureau, Xiamen, China, [2]Laboratory for Climate and Ocean-Atmosphere Studies, Department of Atmospheric and Oceanic Sciences, School of Physics, Peking University, Beijing, China, [3]State Key Laboratory of Marine Environmental Science, College of Ocean and Earth Sciences, Xiamen University, Xiamen, China

Abstract This study examined synoptic impacts on the occurrence of boundaries and their associated convection during summers from 2012 to 2016 over Hetao Irrigation District in North China, where there is a sharp vegetation contrast. Objective synoptic-pattern classification showed that boundary days, especially convective boundary days, were more frequent under a mid-troposphere high-pressure ridge or pre-trough pattern. Such patterns featured a warmer near-surface environment, stronger southerly winds, larger convective available potential energy (CAPE), and low-level moisture convergence. Relative to unfavorable patterns, boundaries under favorable patterns showed more apparent arid-area dependence, more dominant orientation along the line of vegetation contrast, more moved northward, formed and matured earlier, and triggered convection more dispersedly. Under each pattern, compared with nonboundary days, boundary days possessed higher near-surface temperatures and stronger ambient flows against the vegetation-contrast-induced circulations near the surface; plus, compared with nonconvective boundary days, convective boundary days possessed stronger updrafts, larger CAPE, and higher moisture and K index.

Plain Language Summary Boundary layer convergence lines (boundaries), which often manifest as fine lines of clear-air radar echoes, are an important mesoscale mechanism of convective initiation. Mesoscale boundaries induced by vegetation heterogeneity are far less well understood than those induced by the contrast between sea or lakes and land, particularly in terms of synoptic impacts on the occurrence of such boundaries and their associated convection. Based on a boundary data set during the five summers from 2012 to 2016 over Hetao Irrigation District (HID)—an area in North China with a sharp contrast in vegetation, mainly between desert and irrigation areas—the aim of the present study was to link these boundaries and their associated convection with different synoptic features via objective synoptic-pattern classification. Results showed that the boundaries were more likely to occur and trigger convection on days when HID was under a high-pressure ridge or pre-trough pattern. The favorable patterns had a warmer environment with stronger southerly flows for boundaries to develop, along with larger convective available potential energy and moisture convergence for boundaries to trigger convection. Their associated boundaries showed more apparent arid-area dependence, more dominant orientation along the vegetation interface, more northward movements, earlier formation and maturity, and more dispersed convection initiation timing.

1. Introduction

Mesoscale boundaries (i.e., boundary layer convergence lines) represent a narrow zone of low-level convergence that can sometimes promote convection initiation (CI) by forcing the air parcels to reach the level of free convection (e.g., Bai et al., 2019; Wakimoto & Murphey, 2010; Weckwerth & Parsons, 2006; Wilson & Schreiber, 1986), and their detection can aid in the success of fine-scale CI nowcasts (e.g., Mueller et al., 2003; Roberts et al., 2012; Wilson & Mueller, 1993). Boundaries commonly arise from differential heating of the Earth's surface (Markowski & Richardson, 2010). Among such boundaries, sea/lake breeze fronts that occur at the landward edge of sea/lake breeze circulations have been studied relatively thoroughly (e.g., Alexander et al., 2018; Kingsmill, 1995; Sills et al., 2011; Wilson & Megenhardt, 1997). In contrast, the boundaries generated by vegetation heterogeneities have received much less attention.

One typical type of vegetation heterogeneity occurs around irrigation areas in arid regions such as deserts, which creates a sharp contrast in vegetation along the desert-irrigation interface. This contrast can induce mesoscale thermal circulations with upward and downward motions located over the arid and irrigated area, respectively. The circulations may cause a lower frequency of cloud formation over the irrigated side than over the arid side—a phenomenon that has been demonstrated over the irrigation area in the bend of the Yellow River and its vicinity in Inner Mongolia, North China (i.e., Hetao Irrigation District; hereafter HID), both through a statistical analysis of satellite observations (Sato et al., 2007) and a numerical experiment (Kawase et al., 2008). Based on 5 years of summertime radar observations, our earlier work (Huang et al., 2019; hereafter H19) examined the general features of boundaries and their associated convection over HID. A total of 323 boundaries were identified in this area, 44% of which were convective. Our results showed that the boundaries—especially the convective boundaries—were more frequent over the arid area than those over the vegetated area, and tended to run parallel to the line of vegetation contrast.

Boundaries and their associated CI can be greatly influenced by synoptic-scale factors, especially near-surface temperatures and ambient flows. Grau et al. (2020) showed that a higher environmental temperature tended to accompany a larger surface temperature difference (ΔT) between land and sea, which contributed to the establishment of sea breeze circulation. Observational (e.g., Atkins & Wakimoto, 1997; Azorin-Molina & Chen, 2008; Grau et al., 2020; Laird et al., 2001) and numerical (e.g., Arritt, 1993; Crosman & Horel, 2010; Seroka et al., 2018; Zhong & Takle, 1993) studies have shown that an opposing (i.e., offshore) synoptic-scale flow, rather than a supporting (i.e., onshore) flow, serves to strengthen sea/lake breeze circulations. For the sea breezes over the Florida peninsula, offshore (onshore) flow days are observed when the east-west ridge axis of the Bermuda high is south (north) of the Florida peninsula (Atkins & Wakimoto, 1997). However, overly strong opposing flow is not beneficial for the formation of sea/lake breezes (Arritt, 1993). Biggs and Graves (1962) proposed that a small magnitude of the Lake Breeze Index, which is proportional to the ratio of the surface wind speed squared to the land-lake ΔT, is beneficial for the establishment of lake breezes.

Similar to sea/lake breeze, mesoscale circulations induced by vegetation heterogeneity can also be affected by synoptic environments. Doran et al. (1995) compared the boundary layer characteristics of 2 days during a field program and found that thermal circulation only occurred on the day with lighter winds of 4–7 m s^{-1}. Idealized large-eddy simulations showed that well-defined vegetation-contrast-induced circulations can only form when the background winds are lower than 2 m s^{-1} and further trigger convection (Lee et al., 2019; Maronga & Raasch, 2012). Also based on idealized simulations, Rochetin et al. (2017) pointed out that circulations will strengthen and become more circular as the background wind decreases, thus optimizing the moisture convergence and cloud formation before CI. However, studies on typical synoptic features for real-world boundaries, especially vegetation-contrast-induced boundaries, and their associated convection, are quite limited in the literature.

As a follow-up to H19, the aim of the present study is to investigate synoptic impacts on the occurrence of boundaries and their associated convection over HID. Section 2 introduces the data and methods. The synoptic pattern preference of boundaries and their associated convection is examined in Section 3, along with the boundary features under different synoptic patterns. Section 4 compares the environmental features among different summertime day types associated with boundaries. A summary is given in Section 5.

2. Data and Methods

2.1. Radar-Based Boundaries Data Set

This study used the boundary data set established in H19. The data set contains 323 boundaries within HID during the five summers (June to August) from 2012 to 2016. The identification of boundaries was based on the reflectivity data collected by the China New Generation Doppler Weather Radar at Linhe station (40.73°N, 107.36°E) within HID. A boundary is defined as a linear area of enhanced reflectivity (−5 to 10 dBZ, composited using the lowest two elevation angles) with a width less than 10 km, a length greater than 10 km and a duration of at least 6 min. The 323 boundaries were categorized as 143 (44%) convective boundaries and 170 (56%) nonconvective boundaries, depending on whether or not new convective storms with reflectivity exceeding 30 dBZ developed within 50 km of the boundaries. For each identified boundary, the location, time, orientation, and motion were recorded (if available) for its formation, maximum length, and dissipation (for nonconvective

boundaries) or CI (for convective boundaries; the timing of the first 10 dBZ of the first storm) stages. For details regarding the establishment of this data set, please refer to H19.

2.2. Boundaries-Based Classification of Summertime Days

The 5 years of summertime days were classified into boundary days (BDs) and nonboundary days (NBDs). BDs were those with at least one identified boundary occurring, whereas NBDs were those without any identified boundaries occurring. A BD was further labeled as a convective boundary day (CBD) or nonconvective boundary day (NCBD), depending on whether or not at least one identified convective boundary appeared. There were 194 (42.2%) BDs out of the total 460 summertime days, with 100 days (21.7%) being CBDs.

2.3. Reanalysis Data

ERA5, the fifth generation of ECMWF's atmospheric reanalysis (Hersbach et al., 2020), was used for synoptic pattern classification and analysis of the environmental conditions. ERA5 provides hourly variables on surface and pressure levels, as well as some convective parameters including convective available potential energy (CAPE), total column water, and K index, with a horizontal resolution of 0.25° × 0.25°. In conjunction with ERA5, ERA5-Land provides land surface variables at an enhanced resolution of 0.1° × 0.1°, which has been produced by replaying the land component of the ERA5 climate reanalysis. In this study, ERA5 provided the information on pressure levels and convective parameters, while ERA5-Land was used to assess the near-surface environment.

2.4. Objective Classification of Synoptic Patterns

The obliquely rotated principal component analysis method in T mode (T-PCA) proposed by Huth (1993) was applied to objectively classify the synoptic patterns. T mode means the input data matrix is organized with the grid points in rows and the cases (time realizations) in columns, to find typical synoptic patterns more efficiently. Huth et al. (2008) suggested that the T-PCA method outperforms other objective classification methods in reproducing predefined dominant weather patterns embedded in the data set and deriving classification results that are less sensitive to preset parameters with good temporal and spatial stability. Previous studies have demonstrated successful applications of T-PCA in different regions of China (e.g., Bai et al., 2021; He et al., 2017; Wang et al., 2021; Xu et al., 2020). Following these studies, T-PCA was conducted in this study via the open-source software "cost733class," which was developed within the framework of COST Action 733 "Harmonisation and Applications of Weather Type Classifications for European Regions" (Philipp et al., 2016).

3. Environmental Features in Favorable Versus Unfavorable Synoptic Patterns

3.1. Summertime Synoptic Patterns Over HID

The classification of synoptic patterns was based on the spatial distribution of mean sea level pressure (MSLP) at 0800 LST (after which boundaries began to form substantially, as suggested by H19) during the 2012–2016 summers. The T-PCA classification method was performed for northern China (33°–48°N, 100°–115°E) centered on HID. The synoptic patterns of 460 summertime days were classified into five types—namely, T1 to T5, which were ranked in descending order of occurrence frequency (from 26.1% to 14.1%). The significance of the difference in the composite MSLPs (Figures 1a1–1a5) between the days in each type and during the whole five summers (i.e., mean state) was examined with the Student's *t*-test.

T1, which has the most frequent occurrence, is characterized by significantly higher MSLPs to the east of HID and lower MSLPs to the west (Figure 1a1). Such a juxtaposition in MSLP corresponds to a high-pressure ridge at 500 hPa (Figure S1a1 in Supporting Information S1) and an anticyclonic circulation at 700 hPa to the southeast of HID (Figure S1b1 in Supporting Information S1), facilitating southerly winds. T2 displays a post-trough and pre-high-pressure-ridge pattern in HID (Figures S1a2 and S1b2 in Supporting Information S1), with a wide area of high MSLP to the northwest of HID (Figure 1a2). T3 is a post-trough pattern similar to T2 but with the trough located more to the southwest (Figures S1a3 and S1b3 in Supporting Information S1), resulting in low MSLPs to the east of HID (Figure 1a3). Both T2 and T3 display northwesterly winds in HID at both 500

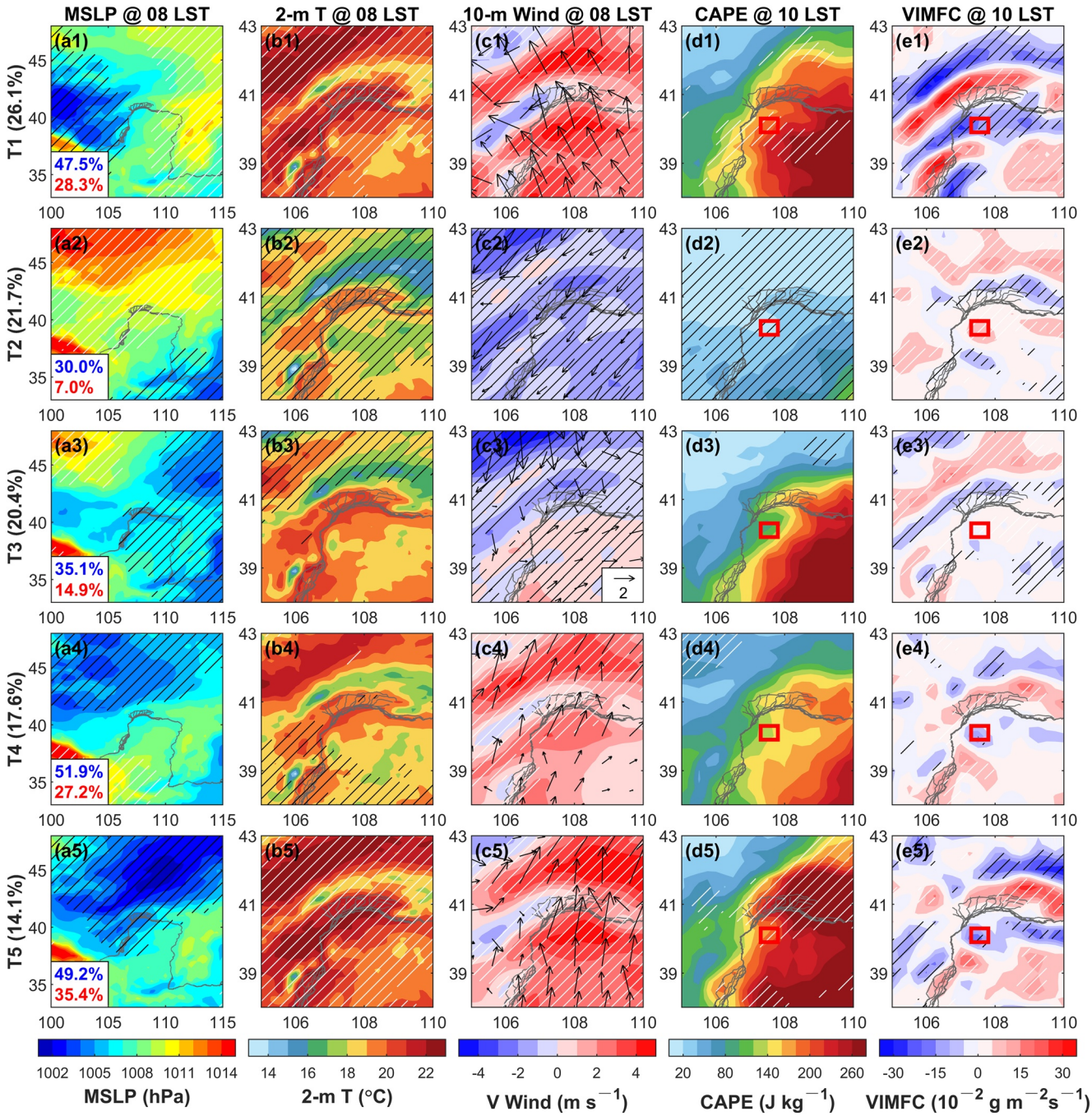

Figure 1. ERA5/ERA5-Land-based composite (a1–a5) mean sea level pressure (MSLP, hPa) at 0800 LST, (b1–b5) 2-m temperature (°C) at 0800 LST, (c1–c5) 10-m winds (m s^{-1}) at 0800 LST, (d1–d5) convective available potential energy (CAPE, J kg^{-1}) at 1000 LST, and (e1–e5) vertically integrated moisture flux convergence (VIMFC, g m^{-2} s^{-1}; from 850 to 750 hPa) at 1000 LST, for the five classified synoptic patterns (i.e., T1–T5) during the five summers from 2012 to 2016. T1–T5 are ranked in descending order of occurrence frequency, given in the black text on the left-hand side. The Yellow River is denoted by gray curves. The white (black) hatched areas in each panel indicate where the composite values are significantly higher (lower) than the mean state during all five summers, as determined by the Student's *t*-test at a confidence level of 90%. The blue (red) number in the lower-left corner of (a1–a5) indicates the occurrence frequency of boundary days (convective boundary days) in each synoptic pattern. In (c1–c5), the wind bars denote the 10-m wind vectors and shaded contours denote the meridional components. In (d1–d5) and (e1–e5), the red boxes denote the key areas of convection associated with boundaries, adapted from Huang et al. (2019).

and 700 hPa (Figures S1a2, S1a3, S1b2, and S1b3 in Supporting Information S1). The MSLPs in T4 and T5 are significantly lower than the mean state, while the low center in T5 is stronger and located more to the east (Figures 1a4 and 1a5). Accordingly, a shallow and deep trough presents in T4 (Figures S1a4 and S1b4 in Supporting Information S1) and T5 (Figures S1a5 and S1b5 in Supporting Information S1) with a 700-hPa trough base

located to the northwest and north of HID, respectively. Winds in HID at 700 hPa are more from the west in T4 (Figure S1b4 in Supporting Information S1), and even turn to the northeast in T5 (Figure S1b5 in Supporting Information S1) with the enhancement of the southeastern high-pressure system.

3.2. Synoptic Pattern Preference of Boundaries and Their Associated Convection

The synoptic pattern preference of boundaries and their associated convection was considered by calculating the proportion of BDs and CBDs over all days of each synoptic pattern. It turns out that BDs occur most frequently in T4, with a percentage of 51.9%, followed by T5 (49.2%), T1 (47.5%), T3 (35.1%), and T2 (30.0%). For CBDs, they are most frequent in T5 (35.4%), and then in T1 (28.3%), T4 (27.2%), T3 (14.9%), and T2 (7.0%). Nearly 72% of BDs are CBDs in T5. Consequently, T1, T4, and T5 are regarded as "favorable patterns" for both BD and CBD occurrence, while T2 and T3 are regarded as "unfavorable patterns" owing to the lower frequencies. The favorable patterns contribute to approximately 58% of all summer days. A representative case for each synoptic pattern is given in Figure S2 in Supporting Information S1.

To understand the synoptic pattern preference, the near-surface temperature and ambient flow were investigated. These two factors have been widely recognized as playing the most fundamental role in determining sea/lake breeze occurrence (e.g., Atkins & Wakimoto, 1997; Biggs & Graves, 1962; Grau et al., 2020; Laird et al., 2001), but their impacts on vegetation-contrast-induced boundaries are less well documented.

Overall, the near-surface environment over HID is significantly warmer in T1 and T5, moderate in T4 and T3, and significantly colder in T2 (Figures 1b1–1b5). The mean 2-m temperature at 0800 LST is basically 3°C higher in T1 and T5 than in T2. As suggested in Grau et al. (2020) based on high-resolution satellite observations, a higher environmental temperature tends to accompany a larger land-sea ΔT, which contributes to the establishment of sea breeze circulation. Here, it is difficult to use the global reanalysis data to directly resolve a realistic value of ΔT between the irrigated and arid areas. Instead, the higher-resolution (1 km) MODIS land surface temperature product could be applicable; however, it is only available for entirely clear-sky conditions. Nonetheless, based on the available samples from MODIS, a positive correlation between the ambient temperature and desert-irrigation ΔT over HID can be observed (Figure S3 in Supporting Information S1). Thus, similar to the findings of Grau et al. (2020), we can conclude that the warmer T1 and T5 tend to produce a larger ΔT, thereby favoring BD occurrence, while the coldest pattern (T2) is the most unfavorable.

The near-surface ambient flows over HID are characterized by a dominant southerly component in the favorable patterns versus a northerly component in the unfavorable patterns (Figures 1c1–1c5). Note that most boundaries appear over the desert to the south of the irrigation area (H19; also refer to Figure 2a), as a result of the vegetation-contrast-induced circulations that blow mainly southward or southeastward from the irrigation area to the desert at lower levels (Kawase et al., 2008; Sato et al., 2007). Therefore, the southerly flow is basically in the opposite direction of the circulations at lower levels and appears to favor boundary occurrence, while the northerly flow is basically in the same direction of the circulations at lower levels and appears to suppress the boundary occurrence. This result agrees with previous studies concerning sea (lake) breeze (e.g., Arritt, 1993; Atkins & Wakimoto, 1997; Laird et al., 2001), which showed that an opposing (offshore) ambient flow would converge with the onshore sea (lake) breeze and lead to the enhancement of the horizontal land-sea temperature gradient and sea (lake) breeze frontogenesis. By contrast, a supporting (onshore) ambient flow tends to disturb the temperature gradient and result in sea (lake) breeze frontolysis.

However, overly strong opposing flow might break the circulation driven by the across-interface ΔT (Arritt, 1993). To assess the balance between the forces associated with ambient flow and ΔT, we calculated the ratio of the perpendicular 10-m wind speed squared to the 2-m temperature at 0800 LST over the key areas for boundaries under the three favorable patterns with dominant opposing winds (see Text S1 in Supporting Information S1 for more details). This quantity resembles the Lake Breeze Index, which was proposed to represent the balance of force in controlling the establishment of lake breezes (Biggs & Graves, 1962). The smaller the ratio is, the more favorable the situation will be for boundary formation. On average, the ratio in T4, T5, and T1 is 0.18, 0.32, and 0.40, respectively, which is perfectly inversely correlated with the BD occurrence frequency (51.9%, 49.2%, and 47.5%, respectively). It turns out that BDs are more likely to occur under a weather pattern with a relatively moderate opposing wind (e.g., T4), even though the environment is not so warm (i.e., the ΔT is not so large).

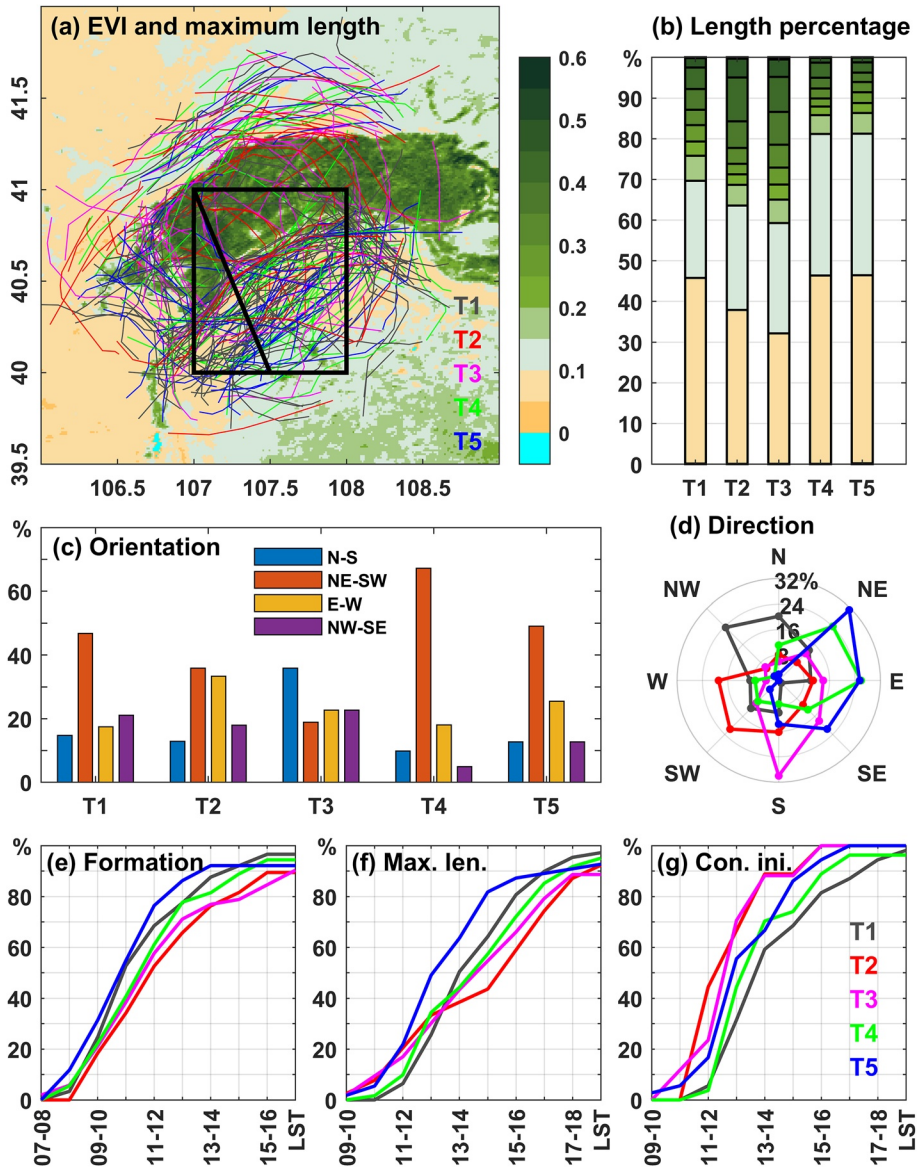

Figure 2. Boundary-related features under different synoptic patterns, including the (a) spatial distribution of boundaries in the stage of maximum length, (b) percentages of boundary lengths in the stage of maximum length over different ranges of enhanced vegetation index (EVI), (c) boundary orientation in the stage of maximum length, and (d) distribution of the direction of movement of boundaries from the formation to maximum-length stage, and (e)–(g) the diurnal cumulative frequency of boundaries in the (e) formation, (f) maximum-length, and (g) convective initiation stage. In (a), the black box denotes the area in which the daily averages for the boxplots in Figure 3 were calculated, and the black line denotes the position of the vertical cross section in Figure S4 in Supporting Information S1. The start time to calculate the diurnal cumulative frequency in (e)–(g) was set at 0700 LST, after which daytime boundaries began to form, as demonstrated by Huang et al. (2019).

Convective conditions were further compared among the synoptic patterns in terms of CAPE and vertically integrated moisture flux convergence (VIMFC; Banacos & Schultz, 2005) from 850 to 750 hPa (almost the lowest 100 hPa over HID) at 1000 LST, after which the boundaries-associated convection became active (H19). Compared to the unfavorable patterns, the favorable patterns have larger CAPE overall (Figures 1d1–1d5) and stronger low-level moisture flux convergence (more negative VIMFC; Figures 1e1–1e5) within HID. In T5 and T1, with the most frequent CBD occurrence, significantly larger CAPE and more negative VIMFC can be seen over the key areas of boundaries-associated convection (red boxes in corresponding figures). The warmer environment under these patterns (Figures 1b1 and 1b5), along with the stronger southerly flows (Figures 1c1

and 1c5), might aid in the enhancement of instability and low-level pooling of moisture. As the weakest of the CBD-preferred patterns, T4 has a relatively moderate CAPE and weaker negative VIMFC. By contrast, the unfavorable types are characterized by smaller CAPE overall and divergent moisture fluxes (positive VIMFC) over HID, especially in T2 with the minimum CBD frequency. These results suggest that boundaries are more likely to trigger convection under a synoptic pattern with higher CAPE and low-level moisture, by further deepening the moist layer and realizing the abundant CAPE.

3.3. Variation in Boundary Features With Synoptic Pattern

Under the favorable patterns, the arid-area-dependence of boundary occurrence suggested in H19 appears to be more remarkable than under its unfavorable counterparts (Figure 2a). This is quantitatively evidenced by a larger proportion of boundaries' maximum lengths over the arid area where the enhanced vegetation index (EVI) is less than 0.15 in T4 (>80%), T5 (>80%), and T1 (~70%) relative to T2 and T3 (~60%) (Figure 2b). Over 20% of boundary lengths in T2 and T3 appear in the irrigation area where the EVI is more than 0.30. These results indicate that the favorable patterns are more conducive to enhancing vegetation-contrast-induced circulations and boundary occurrence within the upward branch of the circulation over the arid side. The boundaries under the favorable patterns apparently preferred the northeast-southwest orientation parallel to the main desert-irrigation interface, with a percentage comparable with (in T1) or larger than (in T4 and T5) the total percentage of other three orientations (Figure 2c). Under the unfavorable patterns, the orientation distribution was relatively even, with the largest percentage less than 40% (Figure 2c). After formation, the boundaries tend to have a more northward component of movement under the favorable patterns (T1, T4, and T5 in Figure 2d), likely due to the dominant southerly ambient flows (Figures 1c1, 1c4, and 1c5); whereas, under the unfavorable patterns, they tend to have a more southward component of movement (T2 and T3 in Figure 2d), probably because of the dominant northerly ambient flows (Figures 1c2 and 1c3).

From a diurnal perspective, the boundaries under the favorable patterns tend to form and obtain their maximum length earlier than those under the unfavorable patterns. Up to 90% of the boundaries in T1, T4, and T5 form before 1500 LST, which is almost 10% higher than those in T2 and T3 (Figure 2e). During the stage of maximum length, the cumulative frequency before 1600 LST ranges from 72% to 87% under the favorable patterns, versus 59% to 66% under the unfavorable patterns (Figure 2f). In addition, all the boundaries in T2 and T3 trigger convection before 1600 LST, with a peak time at midday (1100–1300 LST), as indicated by the largest slope of the line, whereas under the favorable patterns there are some boundaries triggering convection after 1600 LST (Figure 2g). This result indicates that the CI times of the boundaries under the favorable patterns are more dispersive, while the boundaries under the unfavorable patterns are prone to triggering convection around midday, when the thermodynamic environment of the day is relatively favorable.

4. Boundary-Dependent Environmental Features Under Each Synoptic Pattern

This section further compares the environmental characteristics between NBDs and BDs and between NCBDs and CBDs for each synoptic pattern. The comparison is conducted from both the horizontal and vertical viewpoints, respectively covering and across the key areas of boundaries and their associated convection (i.e., the black box and line in Figure 2a).

4.1. Thermodynamic Environment

The near-surface environment is generally warmer on BDs than NBDs for each synoptic pattern, which becomes increasingly apparent from morning to noon as the solar heating strengthens (green vs. blue boxes in Figure 3a). As described above, a warmer environment over HID usually signifies a larger desert-irrigation ΔT, and thus is more likely to drive the occurrence of boundaries. When the environment is sufficiently warm, boundaries tend to trigger convection due to the enhanced convergence along the boundaries (as a result of the large ΔT), as well as the instability of the environment. Accordingly, CBDs consistently have a warmer environment than NCBDs under all five synoptic patterns (red vs. yellow boxes in Figure 3a). For most CBDs (based on the 75% quantile), a 2-m temperature exceeding 21°C, 25°C, and 28°C is the prerequisite at 0800, 1000, and 1200 LST, respectively.

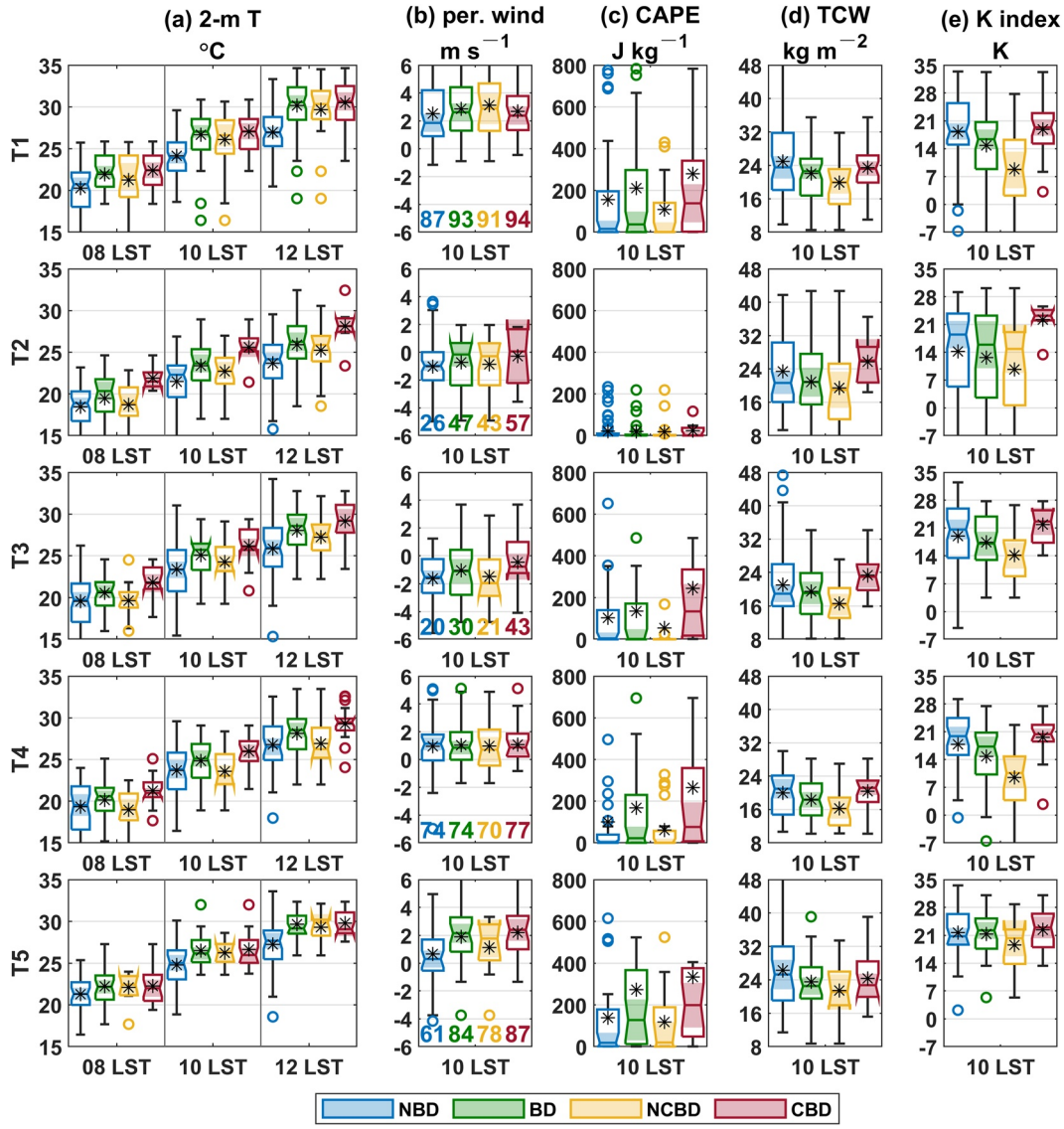

Figure 3. Box-and-whisker plots of the (a) 2-m temperature (°C) at 0800, 1000, and 1200 LST, (b) perpendicular component of 10-m winds (m s^{-1}) at 1000 LST, (c) convective available potential energy (CAPE, J kg^{-1}) at 1000 LST, (d) total column water (TCW, kg m^{-2}) at 1000 LST, and (e) K index (K) at 1000 LST, for comparing NBDs (nonboundary days), BDs (boundary days), NCBDs (nonconvective boundary days), and CBDs (convective boundary days) under the five synoptic patterns (i.e., T1–T5, from top to bottom). For each variable at a time, the daily value is the average over the black box in Figure 2a. The perpendicular component of 10-m winds means the component of 10-m winds along the black line in Figure 2a, roughly perpendicular to the main desert-irrigation interface. The perpendicular wind component is positive when it blows from the desert to irrigation area, and vice versa. The different text colors in (b) represent the percentage (units: %) of positive samples in each boxplot. For each box-and-whisker plot, the top and bottom edges of the box denote the upper and lower quartiles (q_3 and q_1), respectively. The line inside the box denotes the median. The sample outliers, denoted by circles, are the values larger than $q_3 + 1.5\times (q_3 - q_1)$ or smaller than $q_1 - 1.5\times (q_3 - q_1)$. The whiskers above and below each box represent the nonoutlier maximum and minimum, respectively. The asterisk symbols denote the sample averages.

The increasingly warmer environment from NBDs, to NCBDs to CBDs can also be seen in the vertical direction (colored in Figure S4 in Supporting Information S1) from the near-surface to the mid-troposphere close to 500 hPa, although the distinction is less apparent in the higher levels. In addition, even though the desert-irrigation ΔT is hard to realistically resolve using the reanalysis data, it is still faintly visible at lower levels on BDs, and especially on CBDs (Figures S4b1–S4b5 and S4c1–S4c5 in Supporting Information S1).

The development of boundaries under different synoptic patterns may need different desert-irrigation ΔT values. CBDs have a significantly higher near-surface temperature than NBDs throughout T1–T5 (little-to-no notch overlap in the boxplots, especially after 1000 LST), while the temperature distinction between NCBDs and NBDs is apparent only in T1 and T5. These results indicate that the stronger opposing ambient flows in T1 and T5 require a larger desert-irrigation ΔT to achieve a small balance ratio index.

4.2. Ambient Flow

The ambient winds perpendicular to the main desert-irrigation interface, either the opposing (positive) or supporting (negative) winds to the vegetation-contrast-induced circulations, were examined (Figure 3b). Under each pattern, BDs appear to have a larger percentage with opposing flows than NBDs, despite the difference being not too remarkable (green vs. blue values in Figure 3b). The percentages with opposing flows are slightly (3%–9%) more on CBDs than on NCBDs for T1, T4, and T5, and moderately (14%–22%) more for T2 and T3 (red vs. yellow values in Figure 3b).

The perpendicular ambient flows under the favorable patterns are roughly southeasterly and appear to weaken from the desert to the irrigation area, likely owing to the opposite direction of the irrigation-area breezes (arrows in Figure S4 in Supporting Information S1); whereas the perpendicular ambient flows under the unfavorable patterns are roughly northwesterly and appear to enhance from the desert to the irrigation area, probably because of the same direction of the irrigation-area breezes. This is consistent for NBDs, NCBDs and CBDs. The opposing flows over the desert might extend to 650 hPa in T1 (Figures S4a1–S4c1 in Supporting Information S1), but are confined to below 800 hPa in T4 (Figures S4a4–S4c4 in Supporting Information S1) and T5 (Figures S4a5–S4c5 in Supporting Information S1). The upward flows, mainly occurring between 850 and 700 hPa over the desert, are generally more active on CBDs than on NBDs and NCBDs, which might aid in the development of convection on CBDs.

4.3. Convective Parameters

As expected, convective parameters perform well in differentiating CBDs from NCBDs. In terms of CAPE (Figure 3c), the median is significantly larger on CBDs relative to NCBDs for each synoptic pattern, with little-to-no box notch overlap of each box pair. Except in T2, the synoptic patterns possess a mean CAPE value of ∼300 J kg^{-1} on CBDs, versus a value of ∼100 J kg^{-1} or less on NCBDs. Meanwhile, the moisture content is more abundant on CBDs than on NCBDs, as evidenced by the overall higher total column water (Figure 3d) on CBDs, with an average of 20–26 kg m^{-2} versus 16–22 kg m^{-2} on NCBDs. Overall, the average specific humidity on CBDs (green contours in Figures S4c1–S4c5 in Supporting Information S1) is 1–2 g m^{-2} higher than on NCBDs (green contours in Figures S4b1–S4b5 in Supporting Information S1), at the same levels below the mid-troposphere. The K index (Figure 3e), which is a measure of convective potential by combining the temperature lapse rate and lower-tropospheric moisture conditions (American Meteorological Society, 2021), is significantly higher on CBDs than on NCBDs. Without much overlap between the box pairs, the K index seems to be an effective parameter for differentiating CBDs from NCBDs under most synoptic patterns, except T5, in which the K index on NCBDs is only slightly lower than on CBDs.

However, the convective parameters are incapable of distinguishing BDs from NBDs. On the whole, the CAPE values on BDs are only slightly larger than their NBD counterparts, due to the fairly low CAPE values of NCBDs out of BDs (Figure 3c). The total column water (Figure 3d) and K index (Figure 3e) on BDs are comparable to that on NBDs, with the NBD values generally being between those of the NCBDs and CBDs, which can also be seen from the vertical perspective in terms of composite specific humidity (green contours in Figure S4 in Supporting Information S1). These results suggest that convective parameters may not be very helpful in determining whether or not a boundary will occur, but are quite helpful in determining whether or not a boundary will trigger convection once it has occurred.

5. Conclusions

The influences of synoptic features on the occurrence of mesoscale boundaries and their associated convection over HID—an area in North China with a sharp contrast in vegetation (mainly between irrigation and desert areas)—were investigated during the five summers from 2012 to 2016. The summertime days were categorized into BDs and NBDs; and BDs were further divided into CBDs and NCBDs. The daily atmospheric circulations in these five summers were classified into five distinct synoptic patterns based on an objective classification method (T-PCA).

Three synoptic patterns (T4, T5, and T1) that contributed to ~58% of the summer days were found to be favorable for both BD and CBD occurrence. Under the most frequent one of these three patterns, HID was dominated by a high-pressure ridge. Under the other two patterns, HID was located pre-trough (either shallow or deep trough). The two unfavorable patterns were both post-trough with different trough locations. Compared with the unfavorable patterns, the favorable patterns were characterized by a warmer near-surface environment over HID with dominant southerly ambient flows opposite to the irrigation-area breeze of the desert-irrigation circulations, which might have enhanced the circulations and resulted in more frequent BD occurrence. Consistent with the features of the Lake Breeze Index proposed in a previous study, the ratios of the perpendicular 10-m wind speed squared to the 2-m temperature under the three favorable synoptic patterns were found to inversely correlate well with the BD occurrence frequencies in HID with sharp vegetation contrast.

It was also found that the larger CAPE and stronger low-level moisture flux convergence under the favorable patterns may have contributed to the active occurrence of CBDs. Under each synoptic pattern, BDs, and especially CBDs, tended to have a warmer environment and more opposing ambient flows than NBDs. Moreover, CBDs can be successfully distinguished from NCBDs based on their significantly stronger upward flow, larger CAPE, and higher moisture content and K index.

Under the favorable patterns, the boundaries tended to show more apparent arid-area dependence in terms of spatial distribution, were more dominantly orientated along the main desert-irrigation interface, more moved northward, formed and obtained their maximum length earlier, and had a more dispersive CI time.

Despite this study having supplemented H19 by relating the behaviors of mesoscale boundaries with synoptic impacts, the finer-scale effects, such as those from the surface sensible/latent heat flux gradient across the area of vegetation contrast (Kawase et al., 2008), have not been addressed, mainly because of the limitations imposed by the sparseness of observations over HID. A field experiment over this region to fill this knowledge gap is necessary, which our group is planning to carry out in the summer of 2022.

Data Availability Statement

The ERA5/ERA5-Land reanalysis data were provided by ECMWF and downloaded from the Copernicus Climate Change Service Climate Data Store (https://doi.org/10.24381/cds.bd0915c6; https://doi.org/10.24381/cds.adbb2d47; https://doi.org/10.24381/cds.e2161bac). The radar data were provided by the National Meteorological Information Center of the China Meteorological Administration (http://data.cma.cn/data/cdcdetail/dataCode/J.0012.0001P.html; only available in Chinese). The MODIS data were downloaded from NASA's Earth Observing System Data and Information System (EOSDIS; https://doi.org/10.5067/MODIS/MOD11A1.006; https://doi.org/10.5067/MODIS/MOD13A3.006).

Acknowledgments
This study was sponsored by the National Natural Science Foundation of China (Grants 42030604 and 41905049) and the Xiamen Science and Technology Program (Grant 3502Z20206079).

References

Alexander, L. S., Sills, D. M. L., & Taylor, P. A. (2018). Initiation of convective storms at low-level mesoscale boundaries in Southwestern Ontario. *Weather and Forecasting*, *33*(2), 583–598. https://doi.org/10.1175/waf-d-17-0086.1

American Meteorological Society. (2021). K index. Glossary of Meteorology. Retrieved from https://glossary.ametsoc.org/wiki/K_index

Arritt, R. W. (1993). Effects of the large-scale flow on characteristic features of the sea breeze. *Journal of Applied Meteorology and Climatology*, *32*(1), 116–125. https://journals.ametsoc.org/view/journals/apme/32/1/1520-0450_1993_032_0116_eotlsf_2_0_co_2.xml

Atkins, N. T., & Wakimoto, R. M. (1997). Influence of the synoptic-scale flow on sea breezes observed during CaPE. *Monthly Weather Review*, *125*(9), 2112–2130. https://journals.ametsoc.org/view/journals/mwre/125/9/1520-0493_1997_125_2112_iotssf_2.0.co_2.xml

Azorin-Molina, C., & Chen, D. (2008). A climatological study of the influence of synoptic-scale flows on sea breeze evolution in the Bay of Alicante (Spain). *Theoretical and Applied Climatology*, *96*(3–4), 249–260. https://doi.org/10.1007/s00704-008-0028-2

Bai, L., Chen, G., Huang, Y., & Meng, Z. (2021). Convection initiation at a coastal rainfall hotspot in South China: Synoptic patterns and orographic effects. *Journal of Geophysical Research: Atmospheres*, *126*(24), e2021JD034642. https://doi.org/10.1029/2021jd034642

Bai, L., Meng, Z., Huang, Y., Zhang, Y., Niu, S., & Su, T. (2019). Convection initiation resulting from the interaction between a quasi-stationary dryline and intersecting gust fronts: A case study. *Journal of Geophysical Research: Atmospheres*, *124*(5), 2379–2396. https://doi.org/10.1029/2018jd029832

Banacos, P. C., & Schultz, D. M. (2005). The use of moisture flux convergence in forecasting convective initiation: Historical and operational perspectives. *Weather and Forecasting*, *20*(3), 351–366. https://journals.ametsoc.org/view/journals/wefo/20/3/waf858_1.xml

Biggs, W. G., & Graves, M. E. (1962). A lake breeze index. *Journal of Applied Meteorology and Climatology*, *1*(4), 474–480. https://journals.ametsoc.org/view/journals/apme/1/4/1520-0450_1962_001_0474_albi_2_0_co_2.xml

Crosman, E. T., & Horel, J. D. (2010). Sea and lake breezes: A review of numerical studies. *Boundary-Layer Meteorology*, *137*(1), 1–29. https://doi.org/10.1007/s10546-010-9517-9

Doran, J. C., Shaw, W. J., & Hubbe, J. M. (1995). Boundary layer characteristics over areas of inhomogeneous surface fluxes. *Journal of Applied Meteorology and Climatology*, *34*(2), 559–571. https://journals.ametsoc.org/view/journals/apme/34/2/1520-0450-34_2_559.xml

Grau, A., Jiménez, M. A., & Cuxart, J. (2020). Statistical characterization of the sea-breeze physical mechanisms through in-situ and satellite observations. *International Journal of Climatology*, *41*(1), 17–30. https://doi.org/10.1002/joc.6606

He, Z., Zhang, Q., Bai, L., & Meng, Z. (2017). Characteristics of mesoscale convective systems in central East China and their reliance on atmospheric circulation patterns. *International Journal of Climatology*, *37*(7), 3276–3290. https://doi.org/10.1002/joc.4917

Hersbach, H., Bell, B., Berrisford, P., Hirahara, S., Horányi, A., Muñoz-Sabater, J., et al. (2020). The ERA5 global reanalysis. *Quarterly Journal of the Royal Meteorological Society*, *146*(730), 1999–2049. https://doi.org/10.1002/qj.3803

Huang, Y., Meng, Z., Li, W., Bai, L., & Meng, X. (2019). General features of radar-observed boundary layer convergence lines and their associated convection over a sharp vegetation-contrast area. *Geophysical Research Letters*, *46*(5), 2865–2873. https://agupubs.onlinelibrary.wiley.com/doi/abs/10.1029/2018GL081714

Huth, R. (1993). An example of using obliquely rotated principal components to detect circulation types over Europe. *Meteorologische Zeitschrift*, *2*(6), 285–293. https://doi.org/10.1127/metz/2/1993/285

Huth, R., Beck, C., Philipp, A., Demuzere, M., Ustrnul, Z., Cahynova, M., et al. (2008). Classifications of atmospheric circulation patterns: Recent advances and applications. *Annals of the New York Academy of Sciences*, *1146*(1), 105–152. https://www.ncbi.nlm.nih.gov/pubmed/19076414

Kawase, H., Yoshikane, T., Hara, M., Kimura, F., Sato, T., & Ohsawa, S. (2008). Impact of extensive irrigation on the formation of cumulus clouds. *Geophysical Research Letters*, *35*(1), L01806. https://doi.org/10.1029/2007gl032435

Kingsmill, D. E. (1995). Convection initiation associated with a sea-breeze front, a gust front, and their collision. *Monthly Weather Review*, *123*(10), 2913–2933. https://journals.ametsoc.org/view/journals/mwre/123/10/1520-0493_1995_123_2913_ciawas_2_0_co_2.xml

Laird, N. F., Kristovich, D. A. R., Liang, X.-Z., Arritt, R. W., & Labas, K. (2001). Lake Michigan lake breezes: Climatology, local forcing, and synoptic environment. *Journal of Applied Meteorology*, *40*(3), 409–424. https://journals.ametsoc.org/view/journals/apme/40/3/1520-0450_2001_040_0409_lmlbcl_2.0.co_2.xml

Lee, J. M., Zhang, Y., & Klein, S. A. (2019). The effect of land surface heterogeneity and background wind on shallow cumulus clouds and the transition to deeper convection. *Journal of the Atmospheric Sciences*, *76*(2), 401–419. https://doi.org/10.1175/jas-d-18-0196.1

Markowski, P., & Richardson, Y. (2010). Air mass boundaries. In *Mesoscale meteorology in midlatitudes* (pp. 115–160).

Maronga, B., & Raasch, S. (2012). Large-eddy simulations of surface heterogeneity effects on the convective boundary layer during the LITFASS-2003 experiment. *Boundary-Layer Meteorology*, *146*(1), 17–44. https://doi.org/10.1007/s10546-012-9748-z

Mueller, C., Saxen, T., Roberts, R., Wilson, J., Betancourt, T., Dettling, S., et al. (2003). NCAR auto-nowcast system. *Weather and Forecasting*, *18*(4), 545–561. https://journals.ametsoc.org/view/journals/wefo/18/4/1520-0434_2003_018_0545_nas_2_0_co_2.xml

Philipp, A., Beck, C., Huth, R., & Jacobeit, J. (2016). Development and comparison of circulation type classifications using the COST 733 dataset and software. *International Journal of Climatology*, *36*(7), 2673–2691. https://rmets.onlinelibrary.wiley.com/doi/abs/10.1002/joc.3920

Roberts, R. D., Anderson, A. R. S., Nelson, E., Brown, B. G., Wilson, J. W., Pocernich, M., & Saxen, T. (2012). Impacts of forecaster involvement on convective storm initiation and evolution nowcasting. *Weather and Forecasting*, *27*(5), 1061–1089. https://doi.org/10.1175/waf-d-11-00087.1

Rochetin, N., Couvreux, F., & Guichard, F. (2017). Morphology of breeze circulations induced by surface flux heterogeneities and their impact on convection initiation. *Quarterly Journal of the Royal Meteorological Society*, *143*(702), 463–478. https://doi.org/10.1002/qj.2935

Sato, T., Kimura, F., & Hasegawa, A. S. (2007). Vegetation and topographic control of cloud activity over arid/semiarid Asia. *Journal of Geophysical Research*, *112*(D24), D24109. https://doi.org/10.1029/2006jd008129

Seroka, G., Fredj, E., Kohut, J., Dunk, R., Miles, T., & Glenn, S. (2018). Sea breeze sensitivity to coastal upwelling and synoptic flow using Lagrangian methods. *Journal of Geophysical Research: Atmospheres*, *123*(17), 9443–9461. https://doi.org/10.1029/2018jd028940

Sills, D. M. L., Brook, J. R., Levy, I., Makar, P. A., Zhang, J., & Taylor, P. A. (2011). Lake breezes in the southern Great Lakes region and their influence during BAQS-Met 2007. *Atmospheric Chemistry and Physics*, *11*(15), 7955–7973. https://doi.org/10.5194/acp-11-7955-2011

Wakimoto, R. M., & Murphey, H. V. (2010). Analysis of convergence boundaries observed during IHOP_2002. *Monthly Weather Review*, *138*(7), 2737–2760. https://doi.org/10.1175/2010mwr3266.1

Wang, C., Zhao, K., Huang, A., Chen, X., & Rao, X. (2021). The crucial role of synoptic pattern in determining the spatial distribution and diurnal cycle of heavy rainfall over the south China coast. *Journal of Climate*, *34*(7), 2441–2458. https://doi.org/10.1175/jcli-d-20-0274.1

Weckwerth, T. M., & Parsons, D. B. (2006). A review of convection initiation and motivation for IHOP_2002. *Monthly Weather Review*, *134*(1), 5–22. https://journals.ametsoc.org/view/journals/mwre/134/1/mwr3067.1.xml

Wilson, J. W., & Megenhardt, D. L. (1997). Thunderstorm initiation, organization, and lifetime associated with Florida boundary layer convergence lines. *Monthly Weather Review*, *125*(7), 1507–1525. https://journals.ametsoc.org/view/journals/mwre/125/7/1520-0493_1997_125_1507_tioala_2.0.co_2.xml

Wilson, J. W., & Mueller, C. K. (1993). Nowcasts of thunderstorm initiation and evolution. *Weather and Forecasting*, *8*(1), 113–131. https://journals.ametsoc.org/view/journals/wefo/8/1/1520-0434_1993_008_0113_notiae_2_0_co_2.xml

Wilson, J. W., & Schreiber, W. E. (1986). Initiation of convective storms at radar-observed boundary-layer convergence lines. *Monthly Weather Review*, *114*(12), 2516–2536. https://journals.ametsoc.org/view/journals/mwre/114/12/1520-0493_1986_114_2516_iocsar_2_0_co_2.xml

Xu, X., Jiang, Z., Li, J., Chu, Y., Tan, W., & Li, C. (2020). Impacts of meteorology and emission control on the abnormally low particulate matter concentration observed during the winter of 2017. *Atmospheric Environment*, *225*, 117377.

Zhong, S., & Takle, E. S. (1993). The effects of large-scale winds on the sea–land-breeze circulations in an area of complex coastal heating. *Journal of Applied Meteorology and Climatology*, *32*(7), 1181–1195. https://journals.ametsoc.org/view/journals/apme/32/7/1520-0450_1993_032_1181_teolsw_2_0_co_2.xml